AGU PUBLICATIONS

Space Weather

RESEARCH ARTICLE
10.1002/2017SW001750

Key Points:
- There are presently 21 operational CXD instruments continuously monitoring proton fluxes at a wide range of magnetic latitude and local time
- The CXD proton data have been cross calibrated against GOES EPS data
- Proton energies >20 MeV are well characterized by the CXD, and integral fluxes are typically within 20–40% of GOES EPS data

Supporting Information:
- Data Set S1
- Data Set S2
- Data Set S3
- Data Set S4
- Data Set S5
- Data Set S6
- Data Set S7
- Data Set S8
- Data Set S9
- Data Set S10
- Data Set S11
- Data Set S12
- Data Set S13
- Data Set S14
- Data Set S15
- Data Set S16
- Data Set S17
- Data Set S18
- Data Set S19
- Data Set S20
- Data Set S21

Correspondence to:
M. R. Carver,
mrcarver@lanl.gov

Citation:
Carver, M. R., Sullivan, J. P., Morley, S. K., & Rodriguez, J. V. (2018). Cross calibration of the GPS constellation CXD proton data with GOES EPS. *Space Weather*, *16*, 273–288. https://doi.org/10.1002/2017SW001750

Received 25 OCT 2017
Accepted 6 FEB 2018
Accepted article online 20 FEB 2018
Published online 30 MAR 2018

Cross Calibration of the GPS Constellation CXD Proton Data With GOES EPS

Matthew R. Carver[1], John P. Sullivan[1], Steven K. Morley[1], and Juan V. Rodriguez[2,3]

[1]Los Alamos National Laboratory, Los Alamos, NM, USA, [2]Cooperative Institute for Research in Environmental Sciences, University of Colorado Boulder, Boulder, CO, USA, [3]National Centers for Environmental Information, National Oceanic and Atmospheric Administration, Boulder, CO, USA

Abstract Accurate proton flux measurements of the near-Earth environment are essential to the understanding of many phenomena which have a direct impact on our lives. Currently, there is only a small set of satellites capable of performing these measurements which makes certain studies and analyses difficult. This paper details the capabilities of the Combined X-ray Dosimeter (CXD), flown on 21 satellites of the Global Positioning System constellation, as it relates to proton measurements. We present a cross calibration of the CXD with the Energetic Particle Sensor (EPS) onboard the Geostationary Operational Environmental Satellite operated by the National Oceanic and Atmospheric Administration. By utilizing Solar Energetic Particle Events when both sets of satellites were operational we have orders of magnitude in flux and energy to compare against. Robust statistical analyses show that the CXD and Geostationary Operational Environmental Satellite flux calculations are similar and that for proton energies >30 MeV the CXD fluxes are on average within 20% of EPS. Although the CXD has a response to protons as low as 6 MeV, the sensitivity at energies below 20 MeV is reduced and so flux comparisons of these are generally worse. Integral flux values >10 MeV are typically within 40% of EPS. These calibrated CXD data sets will give researchers capabilities to study solar proton access to the inner magnetosphere down to $L \sim 4$ near the equatorial plane at high temporal cadence.

1. Introduction

Proton fluxes in the near-Earth environment are dominated by galactic cosmic rays (GCRs) and Solar Energetic Particle Events (SEPEs). While the former provides a relatively constant flux (varying only on the scale of the solar cycle and Forbush decreases), SEPEs can fluctuate widely in energy, flux, and time. It is known that SEPEs above ~1 MeV can readily access the Earth's magnetosphere (Kress et al., 2015), affecting high-latitude commercial aviation through increased high-frequency radio absorption (Sauer & Wilkinson, 2008) and increased levels of radiation exposure (Matthiä et al., 2015; Mertens et al., 2010). Additionally, resources in orbit face increased risk due to these energetic particle fluxes (Baker, 2000; Hu et al., 2009). In terms of space weather one can use integral proton fluxes above various energies to define and describe the strength of an SEPE, with National Oceanic and Atmospheric Administration (NOAA) using operational definitions of 10 protons cm^{-2} sr^{-1} s^{-1} > 10 MeV and 1 proton cm^{-2} sr^{-1} s^{-1} > 100 MeV.

While there have been (and continue to be) many missions that monitor the near-Earth energetic particle fluxes, the ability to combine measurements reliably is hampered by a lack of crossover in operations and energy coverage. With the release of Global Positioning System (GPS) energetic particle data to the general public (Executive Order 13744, 2016; Morley et al., 2017) there is now more than 187 years of satellite data available dating back to 2001 with more being collected every day. This data set encompasses an entire solar cycle and provides measurements across a broad range of energies and latitudes, including regions previously not well sampled (e.g., Adriani et al., 2015; Crosby et al., 2015; Leske et al., 2001). Figure 1 shows the temporal coverage of the satellites equipped with the Combined X-ray Dosimeter (CXD) instrument along with sunspot number to demonstrate available resources within the solar cycle.

However, a caveat with this large data set is that the CXD was not designed for a purely scientific purpose but to monitor the environmental impact on the satellite systems used on GPS in verification of the Limited Test Ban Treaty (United States Treaties and Other International Agreements, 1963), banning nuclear weapons tests in the atmosphere, space, and under water. It is not obvious that the CXD is capable of performing complex scientific measurements with its limited number of overlapping proton energy channels. The cross-calibrated

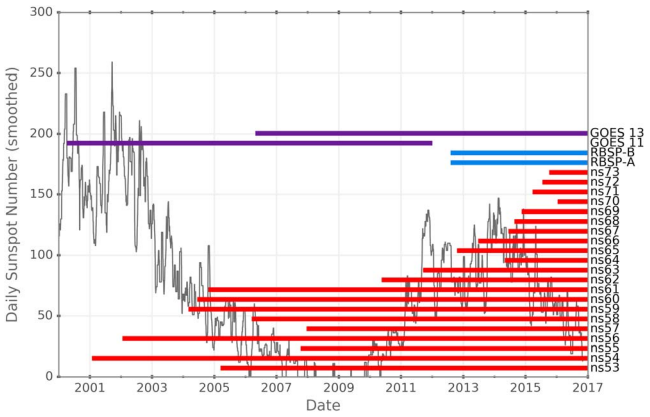

Figure 1. Plot showing daily sunspot number as a function of time from 2000 to 2017 overlaid with a horizontal bar chart showing the coverage of a set of satellites operating energetic proton sensors. Red bars indicate Combined X-ray Dosimeter coverage, magenta represents Geostationary Operational Environmental Satellite Energetic Particle Sensor (GOES EPS) coverage, and blue shows the National Aeronautics and Space Administration Van Allen probes. Modified from Figure 1 of Morley et al. (2017).

data set will allow a number of analyses that were previously impossible to complete without the coverage available with the GPS constellation.

The Geostationary Operational Environmental Satellite (GOES) mission has been in operation since 1974 (18 launched satellites, including the 2 predecessor Synchronous Meteorological Satellites (SMS)) with a primary mission of providing a constant stream of data on atmospheric conditions as well as space weather. While the latter is of most importance to this paper, it is worth noting that the former has been extremely successful in helping track and forecast (potentially deadly) weather with its data and imagery. The operational constellation consists of two satellites positioned on the equator at 75°W and 135°W (GOES East and West, respectively) which provide a comprehensive picture of North and South America and the Atlantic and Pacific Oceans. Additionally, an on-orbit spare is also maintained in the event of a failure of either GOES East or West. The space weather payload called the Space Environment Monitor went through several design changes, with the final version on GOES-13 to GOES-15. It consists of a magnetometer, X-ray sensor, Energetic Particle Sensor (EPS), and starting with GOES-13 an Extreme Ultraviolet Sensor. The Space Environment Monitor has been operational for all SMS and GOES satellites (starting with SMS-1 in 1974) and has provided 98.92 satellite years of data (As of October 2017 calculated with data from https://www.ngdc.noaa.gov/stp/satellite/goes/). The EPS detector design is the same on GOES-8 to GOES-15 (Rodriguez et al., 2014). The length of constant operational coverage combined with validated EPS proton measurements against both the National Aeronautics and Space Administration-Interplanetary Monitoring Platform 8 (Sandberg et al., 2014) and Solar Terrestrial Relations Observatory (STEREO) data (Rodriguez et al., 2017) establishes the EPS data as highly reliable. Coverage of the GOES satellites used for cross calibration is also shown in Figure 1.

This cross calibration is a follow on to the cross calibration of the CXD electron data with the Van Allen probes (Morley et al., 2016). It will adhere to the same procedure with only minor changes dealing with conjunction definition outlined in subsequent sections. First, removing any spectral assumption used in a flux calculation, we will combine EPS flux measurements and CXD instrument responses to get an expected CXD count rate for comparisons. Updates to the instrument response will be made then comparisons of flux calculations will be conducted.

2. Data Description

2.1. Data Sources

The GOES mission is located in geostationary orbit on the equatorial plane at an altitude of approximately 35,800 km. Proton measurements are obtained using EPS which has seven proton channels with effective energies ranging from 1.76 to 148 MeV. The effective energies used in this analysis were derived by Sandberg et al. (2014) for GOES-11 and validated against STEREO measurements by Rodriguez et al. (2017), showing significant deviation from the NOAA Space Weather Prediction Center operational product of integral proton fluxes, becoming more pronounced as proton energy increases. Following Rodriguez et al. (2017), integral fluxes are calculated by summing individual integrals over piecewise power laws representing the differential number flux spectrum defined by the characteristic effective energies of each channel. These integrals are truncated at 500 MeV which includes power law extrapolation beyond the highest energy channel of 148 MeV. The CXD integral fluxes used later in this paper are also truncated at this value to ensure proper comparisons. A full description of the EPS instrument is given by Panametrics (1979, 1980). The EPS data used in this paper come from the westward facing detectors on both GOES-11 and GOES-13 which cover the full time range of data available from the CXD. Sandberg et al. (2014) could not determine effective energies for GOES-13 since it did not overlap with IMP-8. The use of GOES-11 effective energies for GOES-13 is justified by the small differences between GOES-11 and GOES-13 (Using the method of Rodriguez et al., 2014, the differences between EPS channels P2–P7 from GOES-11 and GOES-13B, the westward facing

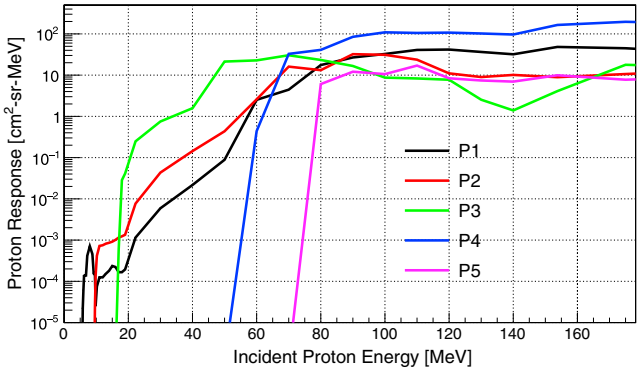

Figure 2. Representative proton response as a function of incident proton energy for each of the five proton channels used in the Combined X-ray Dosimeter instruments on board the block IIR Global Positioning System satellites before cross calibration.

detector used here, are 14%, 6%, 4%, 25%, 3%, and 5%, respectively.) The EPS channel backgrounds (including GCRs) are removed empirically (Rodriguez et al., 2017; Appendix A) prior to calculating integral flux.

The GPS satellite constellation is distributed across six orbital planes inclined at 55° above the equator. These orbits are nearly circular at an altitude of 20,200 km with a 12 h period and cross a wide range of magnetic latitudes (Morley et al., 2016). The CXD measures energetic protons with a nominal sampling rate of 240 s using three sensors: the low-energy particle sensor containing two proton channels 6–10 MeV (P1) and 10–50 MeV (P2), the first high-energy X-ray and particle detector with one proton channel 16–128 MeV (P3), and the second high-energy X-ray and particle detector with two proton channels 57–75 MeV (P4) and >75 MeV (P5). These energies are listed as the nominal definitions, but each of the channels does have a response outside these values. A more detailed description of the proton sensor response calculation can be found in Cayton (2004), but a representative set of response curves can be seen in Figure 2. The exact response files used in the analysis are made available in the supporting information of this publication. These calculated responses take collimator, directionality, and space vehicle effects into account, but as will be seen in subsequent sections the low-energy sensitivity of the CXD is still impacted in an adverse way.

The CXD instrument is currently flown on 21 satellites in the constellation and has collected more than 187 satellite years of data combined since 2001, and this number is currently increasing at a rate of ~1 satellite year of data every 2.5 weeks. This makes the CXD data set the largest and densest space-based proton data set in existence, and the current version of the processed data set is available at https://www.ngdc.noaa.gov/stp/space-weather/satellite-data/satellite-systems/gps/. Several details about the satellites used in this analysis are given in Table 1 including the space vehicle number (SVN) which will be referred to later in the article. The spatial distribution of the GPS satellites combined with the continuous, simultaneous measurements of

Table 1
Details of the GPS Constellation Equipped With the CXD Instrument

Catalog #	SVN	International designator	Orbit plane	Block	Data from (mm/yyyy)
41328	ns70	2016-007A	F	IIF	2/2016
41019	ns73	2015-062A	E	IIF	11/2015
40730	ns72	2015-033A	C	IIF	8/2015
40534	ns71	2015-013A	B	IIF	4/2015
40294	ns69	2014-068A	E	IIF	12/2014
40105	ns68	2014-045A	F	IIF	9/2014
39741	ns67	2014-026A	D	IIF	7/2014
39533	ns64	2014-008A	A	IIF	5/2014
39166	ns66	2013-023A	C	IIF	7/2013
38833	ns65	2012-053A	A	IIF	11/2012
37753	ns63	2011-036A	D	IIF	7/2011
36585	ns62	2010-022A	B	IIF	6/2010
32384	ns57	2008-062A	C	IIR-M	1/2008
32260	ns55	2007-047A	F	IIR-M	11/2007
29601	ns58	2006-052A	B	IIR-M	12/2006
28874	ns53	2005-038A	C	IIR-M	10/2005
28474	ns61	2004-045A	D	IIR	11/2004
28361	ns60	2004-023A	F	IIR	7/2004
28190	ns59	2004-009A	C	IIR	3/2004
27663	ns56	2003-005A	B	IIR	2/2003
26690	ns54	2001-004A	E	IIR	2/2001

Note. Modified from Morley et al. (2017). GPS = Global Positioning System; CXD= Combined X-ray Dosimeter; SVN = space vehicle number.

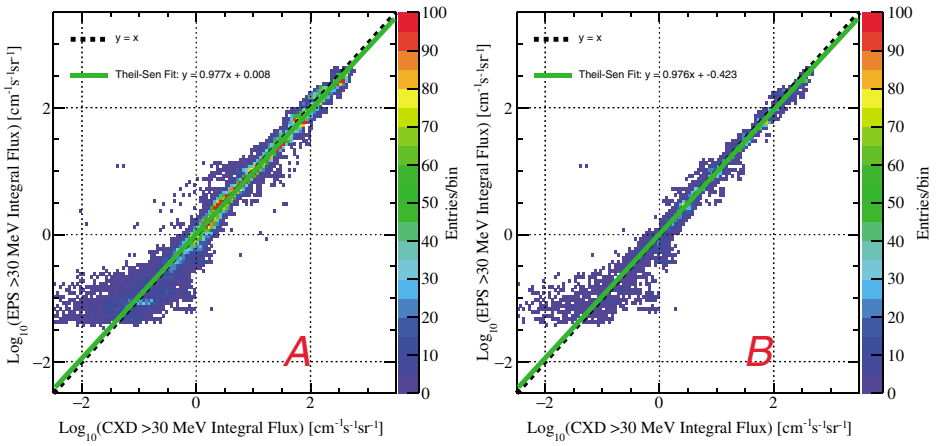

Figure 3. Scatter plots of the $\log_{10}$ of >30 MeV integral flux of Geostationary Operational Environmental Satellite and Combined X-ray Dosimeter (CXD) for a purely temporal conjunction (a) and with the added requirement of a rough spatial connection (b). A $y = x$ line (black dotted line) and a Theil-Sen line (green solid line) of best fit are drawn to show similar behavior between the two situations.

CXD is what gives this data set the advantage over many currently available data. Missions with proton measurement capabilities are usually composed of one or two satellites (Advanced Composition Explorer (Stone et al., 1998), GOES, STEREO (Mueller et al., 2003), Interplanetary Monitoring Platform 8 (Paularena & King, 1999), Payload for Antimatter Matter Exploration and Light-nuclei Astrophysics (PAMELA) (Bonvincini et al., 2001), Radiation Belt Storm Probes (RBSP) (Mauk et al., 2013)). Time History of Events and Macroscale Interactions during Substorms (THEMIS) is an outlier with a five satellite constellation, but its proton detector, the Solid State Telescope, is only sensitive to protons <6 MeV (Angelopoulos, 2008) which does not cover a sufficiently wide range of energy needed for space weather monitoring of SEPEs. It is of course possible to combine measurements from all these missions, but the varying energy coverage and disparate orbits are difficult to reconcile into a coherent data set. In contrast, it is clear that the GPS satellites are easily used in conjunction with each other due to the similarity of both orbit and instrumentation.

2.2. Conjunctions Between GPS and GOES

Due to the low number of SEPEs during Solar Cycle 24, physical conjunctions with the Van Allen Probes as used by Morley et al. (2016) in the CXD electron data cross calibration would only allow validation of the cosmic ray background proton fluxes which do not offer the range of fluxes or energies applicable to space weather research. In contrast, the longevity of the GOES mission coupled with its status as a scientific standard derived through cross calibration with a scientific data set (Sandberg et al., 2014) makes it the optimal choice for our calibration. It was therefore decided that the investigation of SEP intervals would offer the greatest benefit in a cross-calibration procedure. More specifically, highly energetic SEP intervals (peak >10 MeV fluxes of >1,000 cm^{-2} s^{-1} sr^{-1}) are of interest due to their widely varying amount of flux and spectral form allowing us to characterize the fidelity of measurements over this wide range of incident fluxes.

Using SEP intervals with GOES satellites requires assumptions not needed when discussing physical conjunctions. First, over the scale of the Earth (actually 4 and 6.6 Earth radii which are the orbit radii of CXD and GOES, respectively) SEP fluxes are fairly uniform which has been proposed before (Gabriel, 1999) and is tested explicitly below. Additionally, at a sufficient large McIlwain *L*-shell (of which the GPS satellites traverse a wide range due to their inclined orbit), satellites are minimally geomagnetically shielded such that both missions will observe the same fluxes. We therefore define a *temporal* conjunction when (1) GPS satellites are on an *L*-shell >10 and (2) measurements from EPS and CXD are within 2.5 min of each other.

To test these assumptions, we compare fluxes in two situations, the one defined above and one where both satellites are in a rough spatial connection, within ±45° longitude of each other and so above the same quarter of the Earth. The flux obtained by CXD is calculated by fitting all five proton channels simultaneously to a predefined, parameterized flux spectrum as detailed in Appendix A. A comparison of these situations is shown in Figure 3 where the $\log_{10}$ of the >30 MeV integral flux of EPS is plotted against CXD >30 MeV

integral flux for temporal conjunctions (left) and also with the additional requirement of ±45° longitude (right). A robust line of best fit (Theil-Sen estimator (Sen, 1968; Wilcox, 1998)) is shown on each indicating that the behavior of both situations is in agreement. The number of events available using the additional spatial requirement is a factor of ~4 less than without (7,224 conjunctions versus 29,289). For all further plots and analysis we use only temporal conjunctions defined above for increased calibration statistics. With these assumptions made we then look at four separate SEP intervals: December 2006, January 2012, March 2012, and January 2014.

2.3. Description of SEP Intervals

We use a set of four SEP intervals, spanning a total of 45 days and providing ~30,000 conjunctions to perform the cross calibration.

The intervals are those of 5–15 December 2006, 22–31 January 2012, 4–16 March 2012, and 6–14 January 2014. For brevity we refer to these SEP intervals by the month and year of their occurrence throughout the remainder of the manuscript. While CXD-equipped GPS satellites have been on orbit since 2001, the first of 11 Block IIF satellites was launched in May 2010 and the last seven satellites of Block IIF were launched across 2014 and 2015. Large SEP events have occurred rarely in Solar Cycle 24 (Paassilta et al., 2017), and so we have selected these SEP events as they have high peak fluxes (thus spanning a large range of measured flux) as determined by the NOAA Space Weather Prediction Center, are well studied, and were measured by a sufficient number of the CXD instruments.

The SEP interval of December 2006 has been used by a number of previous authors to compare proton flux measurements across different missions (e.g., Lario et al., 2013; Rodriguez et al., 2014, 2017) and had three intensifications in energetic proton flux (e.g., Morley et al., 2017). The first event was associated with X-class flare activity (von Rosenvinge et al., 2009) and showed a slow rise in the proton flux, peaking at an intensity (>10 MeV integral flux) of 1,080 cm^{-2} s^{-1} sr^{-1}. On 13 December a prompt onset of enhanced proton flux associated with a Halo coronal mass ejection (CME) was observed and a subsequent reintensification on 14 December was associated with a second Halo CME (von Rosenvinge et al., 2009). The peak intensity on 13 December was 698 cm^{-2} s^{-1} sr^{-1}, and the SEPE was also detected as a ground-level enhancement (Reames, 2009). The gradual and prompt onset events may have different acceleration mechanisms and spectra (Reames, 1995), thus providing an excellent interval for intercalibration. Seven CXD instruments were operational through this interval, covering Block IIR and Block IIR-M as well as the GOES-11 satellite used for comparison.

The second SEP interval used is that of January 2012 and contains two SEP events. The first event was observed on 23 January with a prompt onset and a peak in the SEPE intensity (6310 cm^{-2} s^{-1} sr^{-1}) associated with the impact of a CME (Nesse Tyssøy et al., 2013). The second event of this interval had a prompt onset on 27 January and was associated with an X-class flare (Gopalswamy et al., 2014). The SEPE intensity at >10 MeV peaked at 796 cm^{-2} s^{-1} sr^{-1}; interestingly, this event was also detected at Mars by the Mars Express spacecraft (Frahm et al., 2013). These events led to disruption of commercial aviation (Copeland et al., 2012) and temporary changes in atmospheric composition, including destruction of mesospheric ozone (von Clarmann et al., 2013). Eleven CXD instruments were operational through this interval, including satellites from Block IIR, IIR-M, and IIF as well as the GOES-13 satellite.

The March 2012 interval is the third used in this study and has been studied in detail as an interval of interest by the Climate and Weather of the Sun-Earth System II Workshop (Tsurutani et al., 2014). The interval begins with a minor enhancement of energetic proton flux that does not exceed the 10 cm^{-2} s^{-1} sr^{-1}threshold required to be identified as a SEPE by NOAA. The 7 March SEPE onset is initially very rapid, followed by a period with a slower rise time, and peaks at an intensity of 6530 $cm^{-2}{\cdot}s^{-1}{\cdot}sr^{-1}$on 8 March. The second onset occurs on 13 March and promptly peaks at an intensity of 469 $cm^{-2}{\cdot}s^{-1}{\cdot}sr^{-1}$. Eleven CXD instruments were operational through this interval, including satellites from Block IIR, IIR-M, and IIF as well as the GOES-13 satellite.

The final interval used here is January 2014. As with the other intervals, more than one SEPE occurred during this period. The interval begins with a small event on 6 January (Kühl et al., 2015) that had a peak intensity of 42 cm^{-2} s^{-1} sr^{-1} at >10 MeV. This event was also associated with an enhancement in >700 MeV flux at geosynchronous orbit, and a ground-level enhancement was observed by the South Pole neutron monitor

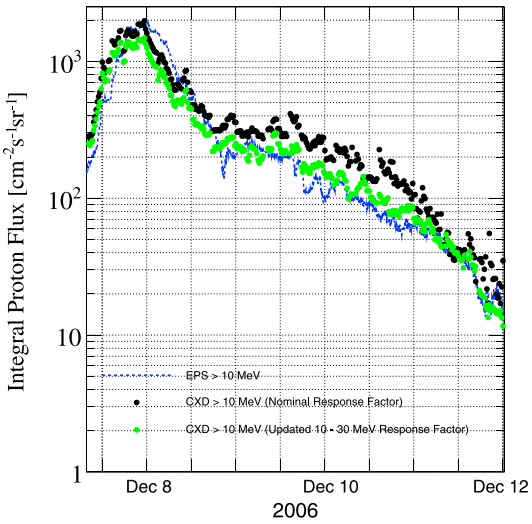

Figure 4. Integral proton flux as a function of day in 2006. Energetic Particle Sensor (EPS) > 10 MeV flux is shown as the blue dotted line, and Combined X-ray Dosimeter (CXD) >10 MeV flux is shown for both the nominal response factor as listed in Table 2 (black dots) and with the additional factor in the 10–30 MeV range (green dots). The details of how the CXD flux values are derived are in Appendix A.

Table 2
List of Response Factors Applied to Each Channel per SVN

SVN	P1	P2	P3	P4	P5
53	1.719	1.419	1.361	1.627	2.101
54	1.918	1.619	1.179	1.669	2.207
55	1.648	1.262	1.156	1.582	1.784
56	1.792	1.524	1.170	1.520	1.779
57	1.686	1.429	0.970	1.519	1.247
58	1.859	1.566	1.256	1.821	2.124
59	1.752	1.417	1.160	1.487	1.606
60	2.101	1.776	1.149	1.631	1.989
61	1.880	1.478	1.063	1.422	1.551
62	1.478	1.482	0.451	0.811	0.611
63	1.462	1.114	0.591	1.110	0.472
64[a]	1.460	1.348	0.624	0.714	0.556
65	1.460	1.348	0.624	0.714	0.556
66	1.335	1.251	0.453	0.710	0.751
67[a]	1.460	1.348	0. 624	0. 714	0.556
68[a]	1.460	1.348	0. 624	0. 714	0.556
69[b]	1.335	1.251	0. 453	0. 710	0.751
70[a]	1.460	1.348	0. 624	0. 714	0.556
71[a]	1.460	1.348	0. 624	0. 714	0.556
72[a]	1.460	1.348	0. 624	0. 714	0.556
73[b]	1.335	1.251	0. 453	0. 710	0.751
Average IIR	1.817	1.499	1.163	1.586	1.821
Average IIF	1.430	1.315	0.549	0.812	0.602

Note. These numbers do not include the additional factor in the 10–30 MeV range to channels P1 (0.3), P2 (0.3), and P3 (2.5). SVN = space vehicle number.
[a]A copy of SVN65. [b]A copy of SVN66.

(Thakur et al., 2014). This prompt SEPE was followed on 7 January by a more gradual onset event with a peak intensity of 1,033 cm^{-2} s^{-1} sr^{-1}. Thirteen CXD instruments were operational through this interval, including satellites from Block IIR, IIR-M, and IIF in addition to the GOES-13 satellite.

3. Results

3.1. Correction of Systematic Offsets

With the set of conjunctions as defined in section 2.2 we may begin to cross calibrate the CXD instrument. As was demonstrated in the cross calibration of the CXD electron data (Morley et al., 2016), we will first compare the counts observed in the CXD instrument with the expected/simulated counts ($\boldsymbol{C_i}$) in a particular CXD channel ($\boldsymbol{i}$) given the differential flux measurements taken by the GOES EPS ($\boldsymbol{j(E)}$) as described in equation (1)

$$\boldsymbol{C_i} = \int_{\boldsymbol{E}} \boldsymbol{j}(\boldsymbol{E})\boldsymbol{G_i}(\boldsymbol{E})\mathrm{d}\boldsymbol{E} \quad (1)$$

where $\boldsymbol{G_i(E)}$ are the CXD instrument response functions that have been calculated using Monte Carlo simulation (Cayton, 2004). This procedure removes any spectral assumptions inherent to a flux calculation and allows us to apply any needed changes to the response functions, where a needed change is defined as deviation from a $y = x$ line. In such cases an overall response factor is applied to the response function independent of energy which modifies the original according to equation (2) where γ is the response factor.

$$\boldsymbol{G}_{\boldsymbol{i}_{\mathrm{updated}}}(\boldsymbol{E}) = \gamma \boldsymbol{G}_{\boldsymbol{i}_{\mathrm{nominal}}}(\boldsymbol{E}) \quad (2)$$

Additionally, a further scaling of the response functions was applied for all SVNs in the 10–30 MeV range by a constant factor (0.3 for channel P1 and P2 and 2.5 for channel P3). This is to account for an average overestimation of the >10 MeV integral fluxes as shown in Figure 4. Because channel P3 overlaps in energy coverage with both P1 and P2 (who also have a response outside their nominally listed energy range) with different levels of sensitivity, it is not a straightforward process to define the appropriate additional scaling. A sampling of different factors in this energy range for all three channels simultaneously yielded the best results with the above factors when comparing the integral flux values of CXD and EPS.

The value of γ for each SVN and channel is shown in Table 2. Some SVNs were not operational during the SEP intervals analyzed, and so response factors, γ, for them are taken from SVNs of a similar block (denoted by superscripts a and b in Table 2). These factors range from a few percent to a factor of ~2 at largest. Additionally, the average response factors for each block of CXD are listed.

Scatter plots of the comparison described above are shown in Figure 5 on a log-log scale with the observed CXD (after the calculated response factors have been applied including the additional scaling in the 10–30 MeV range) on the x axis and the simulated counts from EPS on the y axis. A $y = x$ line has been added along with a Theil-Sen line of best fit to the $\log_{10}$ of the counts. Taking the $\log_{10}$ before the fitting process is required to reduce the heteroscedasticity of the data and to allow the application of ordinary least squares methods (Morley et al.,

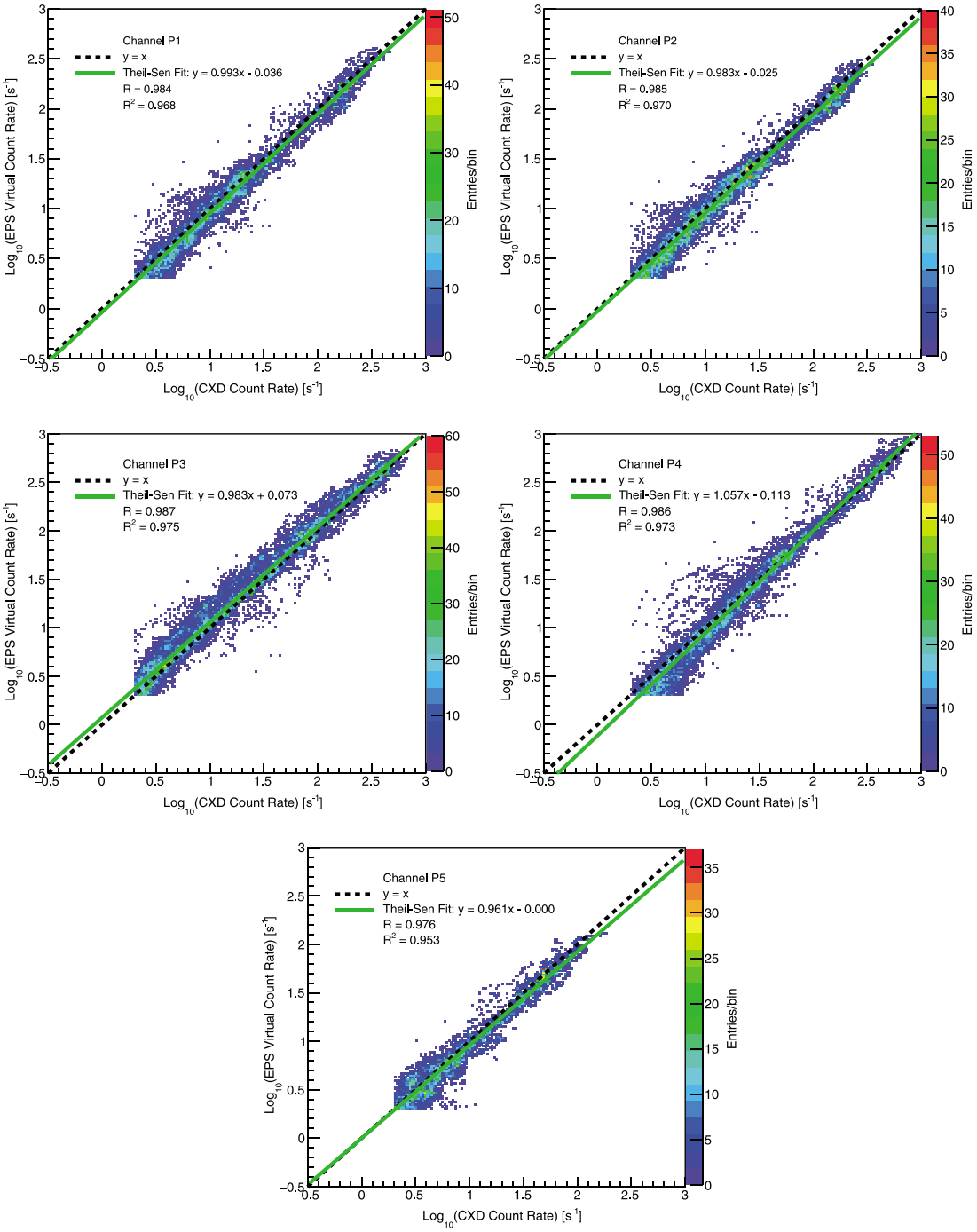

Figure 5. Scatter plot showing the $\log_{10}$ of expected versus observed count rates for all Energetic Particle Sensor (EPS)/ Combined X-ray Dosimeter (CXD) conjunctions where the count rate was >2 counts per second to remove noise/background from the comparison. A $y = x$ line (dotted black) and Theil-Sen line of best fit (solid green) are drawn as well as listing the Pearson correlation coefficient (R) and coefficient of determination (R^2) for each proton channel.

2016). Each plot also lists the Pearson correlation coefficient (R) and the coefficient of determination (R^2). To remove any noise/background floor from either instrument, not expected to follow a linear behavior, only times with >2 counts per second are used. For all channels the lines of best fit have slopes within 5% of unity and spread about this line is minimal across at least 2 orders of magnitude suggesting that the detector responses are of high quality.

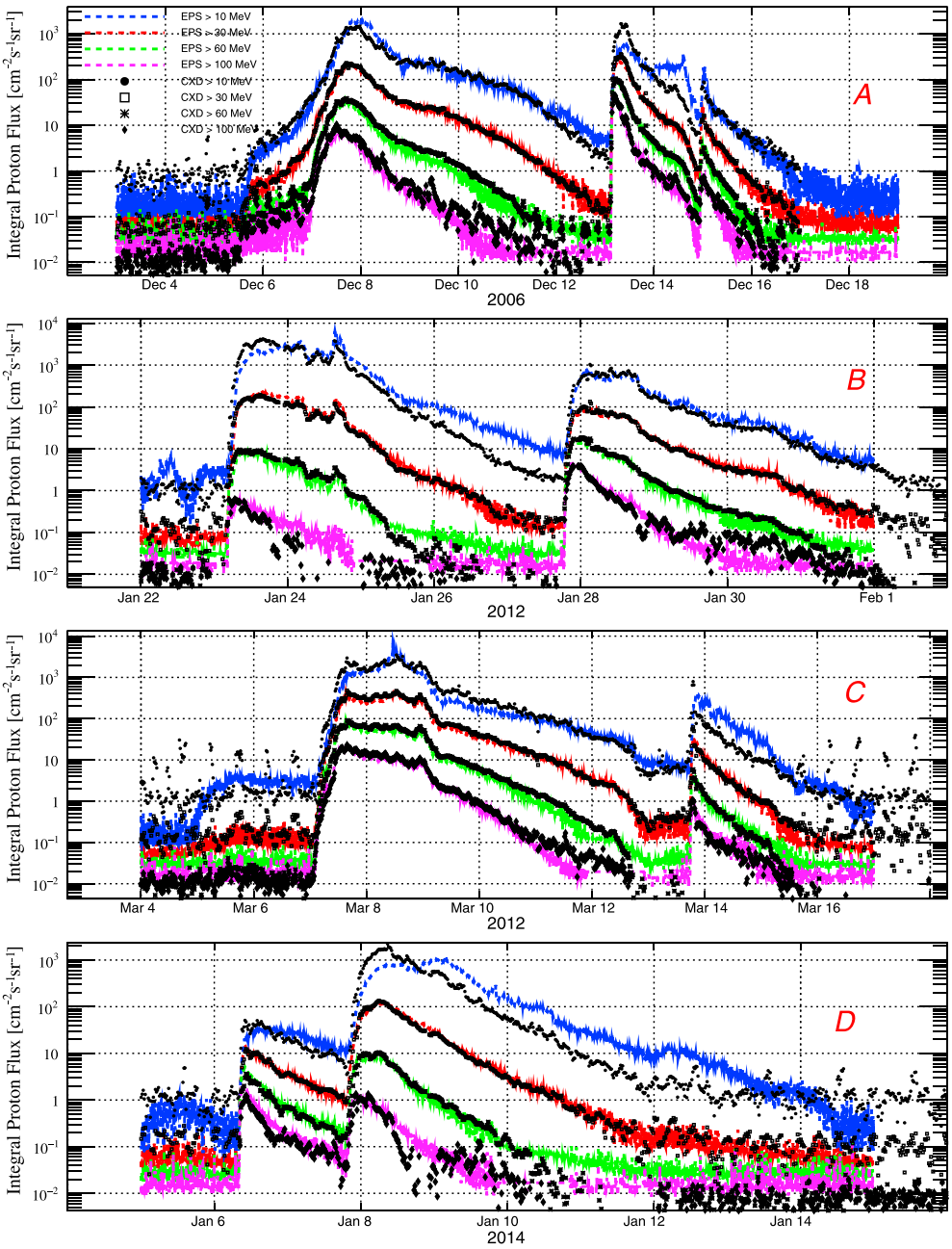

Figure 6. Integral proton flux as a function of day in 2006 (a), 2012 (b and c), and 2014 (d). The Geostationary Operational Environmental Satellite-11 (top) and Geostationary Operational Environmental Satellite -13 EPS 1 min average fluxes are shown as colored dotted lines for >10, >30, >60, and > 100 MeV, while fluxes from all available CXD instruments are shown as black figures listed in legend on 20 min averages.

3.2. CXD Flux Calculation and Comparisons

With the CXD response functions now calibrated as described in the previous section we move on to performing flux calculations for comparison. As we use five proton channels with complicated response functions to estimate the flux spectrum (as detailed in Appendix A), we initially choose to compare against integral flux measurements. The CXD responses have strong peaks at lower energies with a strong integral behavior across higher energies shown in Figure 2. We therefore first compare to another measurement of integral flux and later provide some comparisons of our fitted differential flux spectrum with the

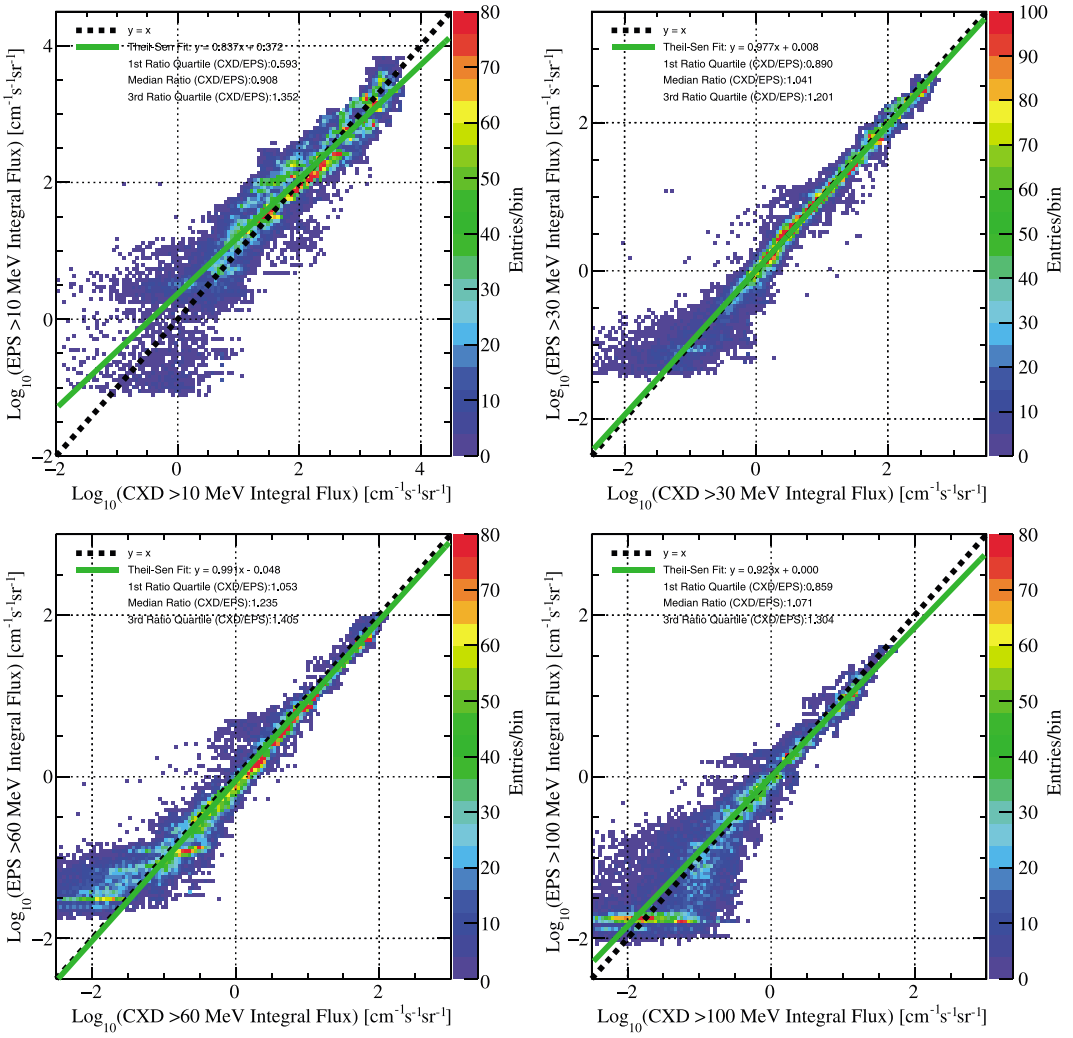

Figure 7. Plot of $\log_{10}$ Geostationary Operational Environmental Satellite-11 and Geostationary Operational Environmental Satellite-13 EPS versus Combined X-ray Dosimeter (CXD) integral proton flux >10 MeV (top left), >30 MeV (top right), >60 MeV (bottom left), and > 100 MeV (bottom right) protons. A $y = x$ line (dotted black), Theil-Sen line of best fit (solid green), and interquartile ranges of the ratio CXD to Energetic Particle Sensor (EPS) fluxes are listed for each.

differential flux data from GOES EPS. Figure 6 shows the integral flux versus time for the four SEP intervals calculated from EPS and all CXD instruments available on a 20 min average. This constitutes anywhere from 7 to 14 combined CXD measurements. Although a quantitative analysis of all intervals is given below, a qualitative description of key areas of agreement/disagreement is beneficial. During the December 2006 interval CXD integral fluxes track well with EPS during the initial gradual onset and through its decay but the >10 MeV CXD fluxes overestimate the secondary prompt onset on 13 December while missing the enhancement beginning on 14 December altogether. This enhancement was observed by both STEREO spacecraft as well as by GOES (Rodriguez et al., 2017). The >30, >60 MeV, and >100 MeV fluxes agree fairly well at all times with EPS, but a trend of >10 MeV CXD integral fluxes agreeing at times and completely disagreeing in others develops in the following SEP intervals. The second prompt onset of the January 2012 interval is well described by CXD including its decay, while the second prompt onset in March 2012 peak is lower by a factor of ~3 as when compared with EPS.

Further, the EPS peak >10 MeV flux in January 2014 contains two separate humps spanning 8 and 9 January while CXD reports a single peak on 8 January that decays at a steady rate. A more detailed discussion on the cause of some of these disagreements is given in the following section.

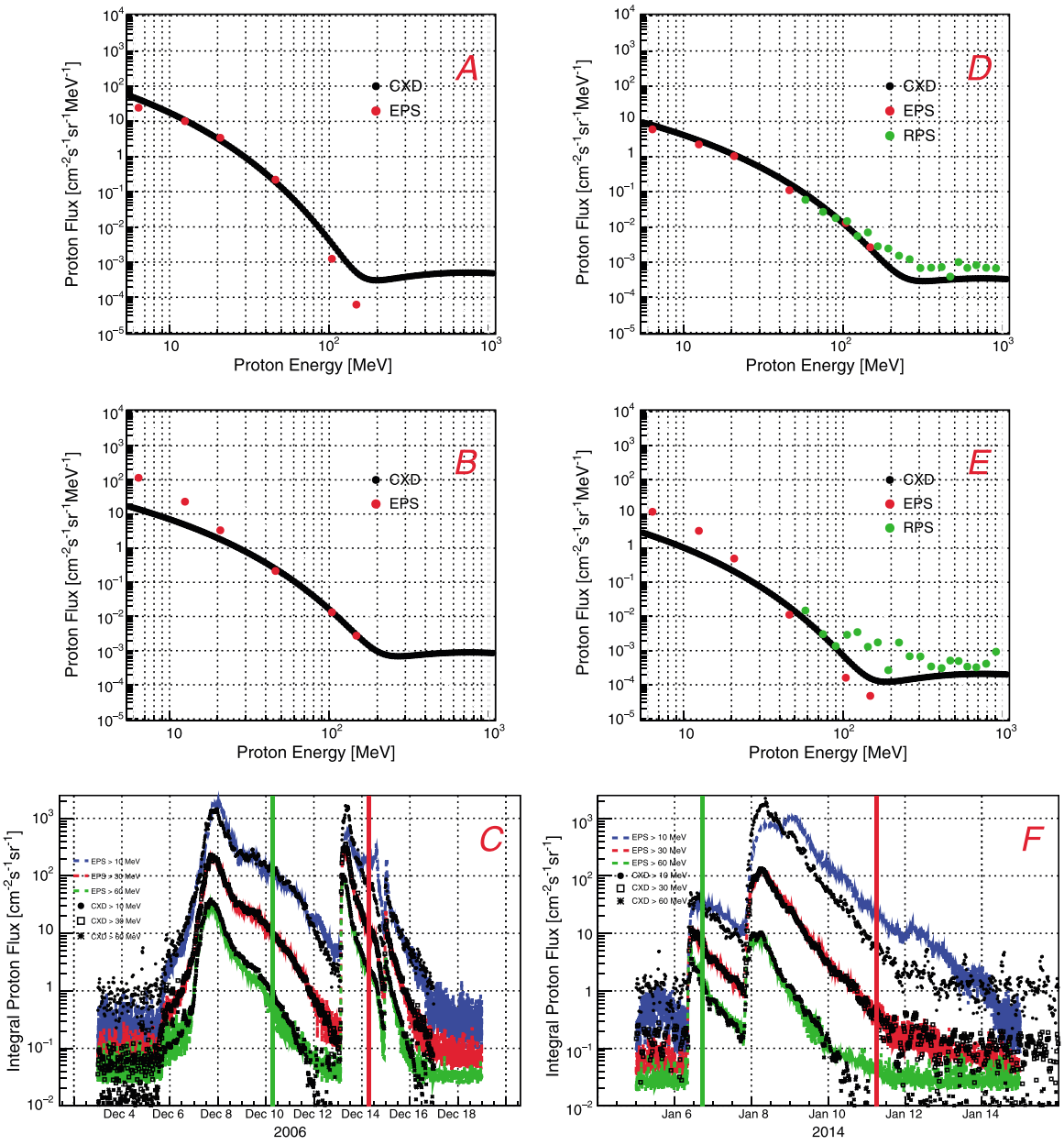

Figure 8. Plots of differential proton flux as a function of proton energy for both times of good and bad agreements. The left column shows times from the December 2006 SEP interval with good (a) and poor (b) agreements with Geostationary Operational Environmental Satellite Energetic Particle Sensor (EPS) and the integral flux versus day (c) highlighting where the energy spectrums are taken with green (good agreement) and red (poor agreement) vertical lines. The right column shows the same good (d) and bad (e) agreements but for the January 2014 SEP interval (f) also including differential measurements from the Van Allen Probes Relativistic Proton Spectrometer (RPS) which were available on this date and have a higher-energy range than EPS. Backgrounds have been removed from EPS while they remain in both Combined X-ray Dosimeter and RPS values which can explain why some EPS points are below Combined X-ray Dosimeter and RPS values at higher energies.

Figure 7 shows scatter plots comparing the $\log_{10}$ of CXD and EPS omnidirectional, integral fluxes where again the $\log_{10}$ of fluxes is used for reasons described above. Lines of best fit are shown on each plot as well as the interquartile ranges of the ratio of CXD to EPS flux. These fits are only done at values larger than the average background subtracted from each of the flux calculations which are 6, 2, 0.5, and 0.125 protons/cm^2 s sr for the >10, >30, >60 MeV, and >100 MeV fluxes, respectively. This ensures that data above background levels are being compared for both instruments. It is clear that the >30, >60, and >100 MeV integral fluxes agree quite well. While the >10 MeV integral fluxes correlate well, they do not agree at the same level; the >30 and >60 MeV lines are in agreement with a slope of unity, while the >10 MeV fit has a slope of 0.84. Additionally,

Table 3
Table of Interquartile Ranges for Both Integral Flux Ratios (CXD/EPS) and Log10 of Ratios

Integral energy	>10 MeV	>20 MeV	>30 MeV	>60 MeV	>100 MeV
Ratio first quartile	0.593	0.693	0.890	1.053	0.850
Log_{10} first quartile	−0.227	−0.160	−0.050	0.022	−0.071
Ratio median	0.908	0.904	1.041	1.235	1.071
Log_{10} median	−0.042	−0.039	0.018	0.092	0.030
Ratio third quartile	1.352	1.107	1.201	1.405	1.304
Log_{10} third quartile	0.131	0.044	0.080	0.148	0.115

Note. CXD= Combined X-ray Dosimeter; GOES = Geostationary Operational Environmental Satellite.

there is a significant spread of values around the $y = x$ line. Although the highest density of points on the >10 MeV flux is centered on the $y = x$ line, there is a significant population off of this line. The spread around the >100 MeV flux only becomes significant at levels below the NOAA operational definition of an SEP event.

Figure 8 shows the energy spectrum of the CXD proton flux as compared with the differential measurements of EPS in times of both good and bad agreements for both the Block IIR and IIF satellites. Differential fluxes from the Relativistic Proton Spectrometer (RPS) (Mazur et al., 2012) onboard the Van Allen Probes are also shown for one SEP interval when data were available (January 2014). Data from RPS are subject to the same temporal conjunction requirements as EPS and CXD as outlined in section 2.2 with a relaxation on *L*-shell requirement to >5.5 because the apogee of the Van Allen Probes is only at an *L*-shell of ~6. Backgrounds have been removed from EPS, while they remain in both CXD and RPS values which can explain why some EPS points are below CXD and RPS values at higher energies.

3.3. Discussion and Interpretation

Despite the less than perfect agreement, on average all integral fluxes agree well. A listing of interquartile ranges shows that the median ratio (CXD/EPS) is 0.90, 0.90, 1.04, 1.23, and 1.08, and the CXD data within the first and third interquartile ranges are within 40%, 30%, 20%, 40%, and 30% of EPS fluxes for the >10, >20, >30, >60, and >100 MeV integral fluxes, respectively. Additionally, we quote the interquartile ranges of the $\log_{10}$ of the ratio (CXD/EPS) listed in Table 3 along with pure ratios. We do this as a factor of two difference that has the same magnitude for overestimate and underestimate using $\log_{10}$ (CXD/EPS), but the same is not true for the untransformed ratio (see, e.g., Morley et al., 2016). The spread around the median value significantly decreases as proton energy increases but remains stable after the 30 MeV while the median ratio value increases with energy, peaking at 1.23 for >60 MeV and returns to less than 1.1 for >100 MeV.

We further express the bias in the CXD fluxes, as compared with GOES, as a percentage. Rather than using the mean percentage error, which penalizes overprediction more heavily than underprediction, we follow the approach given in Morley et al. (2018) to obtain a percentage bias from the $\log_{10}$ of the flux ratio that is then symmetric with respect to overprediction and underprediction as given by

$$\text{Bias} = \mathbf{100}\,\text{sign}(\boldsymbol{MdLQ})\left(\boldsymbol{e}^{|\boldsymbol{MdLQ}|} - \mathbf{1}\right) \tag{3}$$

where

$$\boldsymbol{MdLQ} = \text{Median}[\log(\boldsymbol{Q})] \tag{4}$$

and $\boldsymbol{Q}$ is the ratio of fluxes (CXD/EPS). The bias for the >10, >20, >30, >60, and >100 MeV integral fluxes are −10.2%, −10.6%, 4.1%, 23.5%, and 7.1%, respectively. While the broad strokes of what these values mean is captured by both the median ratio and percentage bias, namely, that a bias exists in one direction or the other, the comparison of these biases is symmetric using the percentage bias with the difference from a pure ratio becoming more pronounced at values far from 1.

An explicit comparison of EPS integral flux with CXD observed count rates gives some explanation of the disagreement in >10 MeV flux calculation. Figure 9 shows the EPS and CXD > 10 and >30 MeV integral fluxes plotted with the counts from the P1, P2, and P3 channels of CXD (scaled down by a factor of 50

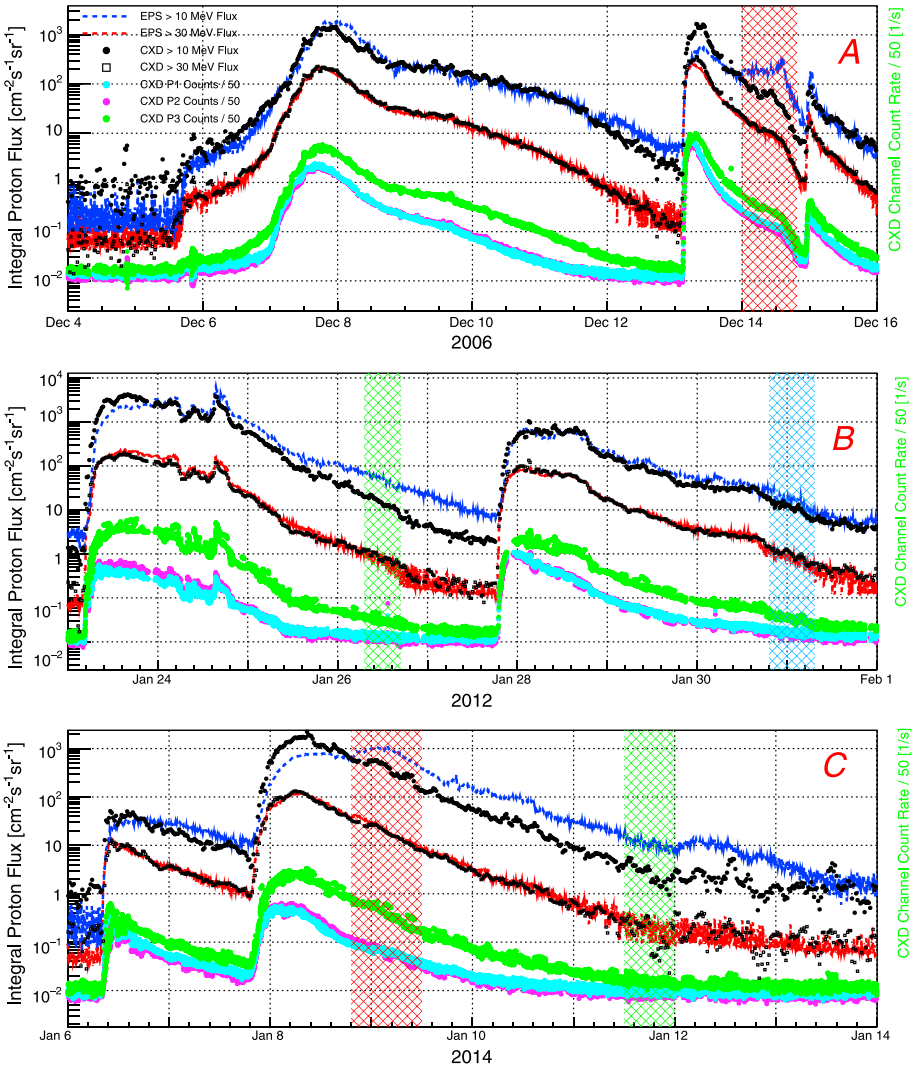

Figure 9. Plot showing both integral flux of Combined X-ray Dosimeter (CXD) and Energetic Particle Sensor (EPS) along with the count rates in channels P1, P2, and P3 of CXD scaled down by a factor of 50 in 2006 (a), 2012 (b), and 2014 (c). The red hatched region shows an area where the EPS flux measurements show structure not present in CXD count rates. The green hatched region shows a time where although CXD flux shares the shape of EPS, the values are significantly less attributed to near-background count rates. The blue hatched region is a time in which the proton channel counts and flux of CXD match reasonably well with the green regions while the EPS fluxes do not.

to separate the shapes). It is clear that the counts are a good proxy for the shape of integral flux. It can also be seen that structures exist in the EPS fluxes that are not present in the CXD counts which gives the instrument no way to reconstruct them in its flux calculation. Examples include the peak in EPS >10 MeV flux beginning on 14 December in the 2006 SEP interval as well as the second hump at the peak of the January 2014 SEP interval beginning just before 9 January which are highlighted by a red hatched area.

Additionally, there are times when the CXD >10 MeV flux is significantly below EPS while still maintaining the same shape as EPS flux. This is seen on the second half of 11 January in the 2014 SEP interval, and the second half of 26 January 2012 SEPE both highlighted with a green hatched area. In both instances, however, the CXD count rate is only marginally above background levels and so calculating a flux that is more than 2 orders of magnitude larger than background is not feasible. Further, Figure 9c shows a second hatched area in blue on 31 January in which the CXD count rates and fluxes match relatively well with the early green hatched area on 26 January. However, the EPS >10 MeV integral flux is significantly different

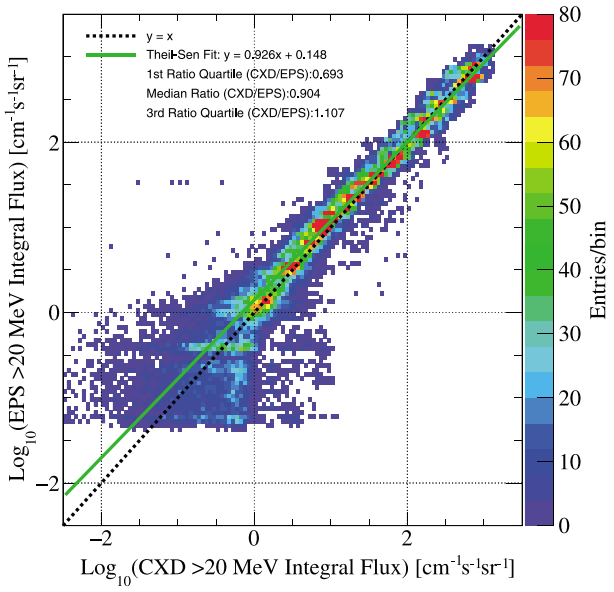

Figure 10. Plot of $\log_{10}$ Geostationary Operational Environmental Satellite-11 and Geostationary Operational Environmental Satellite-13 Energetic Particle Sensor (EPS) versus Combined X-ray Dosimeter (CXD) integral proton flux >20 MeV. A $y = x$ line (dotted black), Theil-Sen line of best fit (solid green), and interquartile ranges of the ratio CXD to EPS fluxes are listed for each.

while the >30 MeV flux matches in both ranges; this indicates that there must be more 10–30 MeV proton counts in EPS on 26 January than available to CXD.

Due to the examples detailed above, we attribute the disagreement in the >10 MeV integral proton fluxes to instrument sensitivity rather than the flux fitting procedure. Because there are cases when the >10 MeV integral flux is larger and smaller than what EPS reports, and so intermittent, this would be a difficult effect to flag for nonuse by a user of the data set. The collimator used on the low-energy particle (Cayton, 2004) is the likely explanation for loss of sensitivity at low proton energies and suggests an issue with directionality of sensors as well. The CXD is nadir pointing (toward Earth), while the EPS looks eastward or westward in the geostationary orbit, depending on the satellite (Rodriguez et al., 2014). (Only fluxes from westward looking EPS instruments were used in the present cross calibrations with CXD in order to minimize the effects of geomagnetic cutoffs.) We therefore recommend that users of the data set restrict their analyses to the >20 MeV integral fluxes to avoid any complications that may arise due to instrument insensitivity at lower proton energies without significant thought into how it may affect their results. This energy value has been chosen by calculating and examining a set of intermediate integral flux values between 10 and 30 MeV with 20 MeV being the lowest energy which shows similar linear fit parameters as the >30 MeV integral flux comparison as seen in Figure 10.

4. Summary and Conclusions

The recent release of energetic particle data from the GPS constellation (Morley et al., 2017) includes proton data. As noted by these authors, the proton data in the initial release had not been cross calibrated against a reference mission. Using the GOES EPS instrument as a source of highly reliable science measurements, we have evaluated the CXD's ability to calculate a differential and integral proton flux. The following are the observations of merit.

1. The CXD provides good quality proton flux measurements across a range of proton energies. For the >10, >20, >30, >60, and >100 MeV integral fluxes the median ratio of CXD to EPS is 0.90, 0.90, 1.04, 1.24, and 1.07, respectively. In addition, the data within the first and third quartile ranges of these same integral flux values are within 40%, 30%, 20%, 40%, and 30%, respectively.
2. While proton response of the CXD extends down to 6 MeV due to collimator holes in instrument filters, the >10 MeV integral proton flux is not well captured as shown by the comparisons with EPS above. We attribute this primarily to instrument sensitivity as opposed to flux fitting procedure and recommend that users of the data restrict their analysis to integral flux values >20 MeV.
3. These calibrated data sets will allow a number of exciting multipoint analyses such as more accurate probing of geomagnetic cutoffs as well as providing additional input to radiation belt climatology models such as AE9/AP9/SPM (Ginet et al., 2013).
4. The new data set will contain the raw count data from the five proton channels, differential and integral fluxes (with and without background subtraction), at a variety of energies starting at >10 MeV and also the fit parameters such that a differential/integral flux may be calculated at any energy. This is different from the currently released data set which only had proton channel rates and uncalibrated fluxes at high McIlwain L.

Appendix A: Flux Fitting Procedure

The fit function used is a combination of an exponential spectrum in momentum which models the SEPEs combined with a Gaussian in log(momentum) to describe the cosmic background (defined below in equations (A1) and (A2)).

Table A1
Fit Parameters Used in the Fit to the CREME96 Simulation of Galactic Cosmic Ray Background

Parameter	A	E_0	σ	B	C
Solar min.	1.076×10^{-4}	3.293×10^{2}	1.305	2.441	3.671×10^{-2}
Solar max.	3.286×10^{-5}	7.463×10^{2}	1.202	2.887	2.467×10^{-2}

$$j_{SEP} = \frac{AN_0}{e^{43.33/r_0}} \left(\frac{E}{p}\right) e^{-\frac{p}{r_0}} \tag{A1}$$

where N_0 is the number density fit, p is the proton momentum (MeV/c), E is total proton energy (MeV), r_0 is the proton momentum fit, 43.33 represents the momentum of a proton with kinetic energy = 1 MeV, and A = 0.046132 is a normalization factor such that the flux is 1,000 protons / (cm^2 s sr MeV) at 1 MeV of kinetic energy. This equation comes from Cayton et al. (2010) which references Freier and Webber (1963).

$$j_{Bkg} = B*[j_1 + f(j_2 - j_1)] \tag{A2}$$

where the fit parameters B and f are an overall normalization and f is a value between 0 and 1 representing some intermediate form of j_n (n representing solar min or max), respectively, described in equation (A3).

$$j_n = A_n e^{-\left[\log\left[E/E_{0n}\right]\right]^2/2\sigma_n} + B_n E^{-C_n} \tag{A3}$$

where the five parameters with the n subscript are a five-parameter fit to the CREME96 (Menderhall & Weller, 2012; Tylka et al., 1997; Weller et al., 2010) simulation of the GCR background at solar min (1) and max (2) at GPS altitude with values given in Table A1.

The fitting procedure is a two-step process, differential in proton energy, in which the SEP contribution is fitted first followed by both the SEP and cosmic background terms. The initial values of N_0 and r_0 are taken to be 0.1 and 200, respectively, as a guess with limits only to ensure positive definiteness. The second fit uses the output of the first for guesses on N_0 and r_0, and the limits on these values are updated to a factor of 10 above and below the guess. Initial guess on B and f is 1 and 0.5, respectively. Limits on B are again only to impose positive definiteness, and limits on f restrict the values to between 0 and 1. After fitting a running average of calculated integral fluxes over the prior 1 week period is subtracted from fitted fluxes to obtain a background subtracted value.

All fitting is performed within the ROOT data analysis package (Antcheva et al., 2009) using the MINUIT minimization package (James & Roos, 1975). Specifically, MIGRAD is the algorithm used for minimization which is a version of the Davidon-Fletcher-Powell formula (e.g., Press et al., 1992) and is minimizing the chi-square distribution of the observed channel counts with respect to the calculated ones which are a function of the fit parameters above and take the derived response factors into account in accordance with equation (1).

Acknowledgments
This work was performed under the auspices of the U.S. Department of Energy. The list of Solar Proton Events, including their timings and peak intensities, prepared by the NOAA Space Weather Prediction Center is available at ftp://ftp.swpc.noaa.gov/pub/indices/SPE.txt.%20The%20version%201.03. The version 1.03 data described by Morley et al. (2017) are available at https://www.ngdc.noaa.gov/stp/space-weather/satellite-data/satellite-systems/gps/ and will be updated to reflect this calibration in the near future. The CXD data used in this publication are available at https://zenodo.org/record/1035934. The GOES-11 and GOES-13 solar proton differential fluxes used as inputs to the analysis in this paper are available at https://satdat.ngdc.noaa.gov/sem/goes/data/new_avg/. The RPS data (version 1.0.1) used in this paper are available at http://virbo.org/ftp/RBSP/RPS/. S. K. M. was supported by the U.S. Department of Energy Laboratory Directed Research and Development (LDRD) award 20150127ER LA-UR-17-30489.

References

Adriani, O., Barbarino, G. C., Bazilevskaya, G. A., Bellotti, R., Boezio, M., Bogomolov, E. A., et al. (2015). PAMELA's measurements of magnetospheric effects on high-energy solar partiles. *Astrophysical Journal Letters*, *801*(1). https://doi.org/10.1088/2041-8205/801/1/L3

Angelopoulos, V. (2008). The THEMIS mission. *Space Science Reviews*, *141*(1-4), 5–34. https://doi.org/10.1007/s11214-008-9336-1

Antcheva, I., Ballintijn, M., Bellenot, B., Biskup, M., Brun, R., Buncic, N., et al. (2009). ROOT—A C++ framework for petabyte data storage, statistical analysis, and visualization. *Computer Physics Communications*, *180*(12), 2499–2512. https://doi.org/10.1016/j.cpc.2009.08.005

Baker, D. N. (2000). The occurrence of operational anomalies in spacecraft and their relationship to space weather. *IEEE Transactions on Plasma Science*, *28*(6), 2007–2016. https://doi.org/10.1109/27.902228

Bonvincini, V., Barbiellini, G., Boezio, M., Mocchiutti, E., Schiavon, P., Scian, G., et al. (2001). The PAMELA experiment in space. *Nuclear Instruments and Methods in Physics Research Section A: Accelerators, Spectrometers, Detectors and Associated Equipment*, *461*(1-3), 262–268. https://doi.org/10.1016/S0168-9002(00)01221-3

Cayton, T. E. (2004). Monte Carlo simulation of the particle channels of the combined X-ray and dosimeter (CXD), Tech. Rep. LA-UR-04-7092, Los Alamos Natl. Lab., Los Alamos N. M. Retrived from http://permalink.lanl.gov/object/tr?what=info:lanl-repo/lareport/LA-UR-04-7092, (accessed date 15 October, 2016)

Cayton, T. E., Chen, Y., Friedel, R. H. W., & Kippen, R. M. (2010). Analysis of electron and proton environment data for medium-Earth orbit (2000-present), LA-UR-10-04234, Los Alamos Natl. Lab., Los Alamos N.M. Retrieved from http://permalink.lanl.gov/object/tr?what=info:lanl-repo/lareport/LA-UR-10-04234, (accessed date 15 October 2016)

Copeland, K. A., Tools, C. A. M. I., & Services for evaluating space weather (2012). Aviation. *Space and Environmental Medicine*, *83*(9), 916–917. https://doi.org/10.3357/ASEM.3462.2012

Crosby, N., Heynderickx, D., Jiggens, P., Aran, A., Sanahuja, B., Truscott, P., et al. (2015). SEPEM: A tool for statistical modeling the solar energetic particle environment. *Space Weather*, *13*, 406–426. https://doi.org/10.1002/2013SW001008

Executive Order 13744 (2016). Executive order—Coordinating efforts to prepare the nation for space weather events. 81 Federal Register, pp. 71,573–71,577.

Frahm, R. A., Sharber, J. R., Winningham, J. D., & Elliot, H. A., et al. (2013). Solar energetic particle arrival at Mars due to the 27 January 2012 solar storm, AIP Conference Proceedings 1539, 394. https://doi.org/10.1063/1.4811068

Freier, P. F., & Webber, W. R. (1963). Exponential rigidity spectrums for solar-flare cosmic rays. *Journal of Geophysical Research*, *68*, 1605–1629. https://doi.org/10.1029/JZ068i006p01605

Gabriel, S. B. (1999). Cosmic rays and solar protons in the near-Earth environment and their entry into the magnetosphere. Proceedings of the workshop on Space Weather, 11 – 13 November 1998, ESA, ESTEC, Noordwijk, The Netherlands, WPP-155, 99–106.

Ginet, G. P., O'Brien, T. P., Huston, S. L., Johnston, W. R., Guild, T. B., Friedel, R., et al. (2013). AE9, AP9, and SPM: New models for specifying the trapped energetic particle and space plasma environment. *Space Science Reviews*, *179*(1-4), 579–615. https://doi.org/10.1007/s11214-013-9964-y

Gopalswamy, N., Xie, H., Akiyama, S., Mäkelä, P. A., & Yashiro, S. (2014). Major solar eruptions and high-energy particle events during solar cycle 24. *Earth, Planets and Space*, *66*(1), 104. https://doi.org/10.1186/1880-5981-66-104

Hu, S., Kim, M.-H. Y., McClellan, G. E., & Cucinotta, F. A. (2009). Modeling the acute health effects of astronauts from exposure to large solar particle events. *Health Physics*, *96*(4), 465–476. https://doi.org/10.1097/01.HP.0000339020.92837.61

James, F., & Roos, M. (1975). Minuit—A system for function minimization and analysis of the parameter errors and correlations. *Computer Physics Communications*, *10*(6), 343–367. https://doi.org/10.1016/0010-4655(75)90039-9

Kress, B. T., Hudsen, M. K., Selesnick, R. S., Mertens, C. J., & Engel, M. (2015). Modeling geomagnetic cutoffs for space weather applications. *Journal of Geophysical Research: Space Physics*, *120*, 5694–5702. https://doi.org/10.1002/2014JA020899

Kühl, P., Banjac, S., Dresing, N., Goméz-Herrero, R., Heber, B., Klassen, A., & Terasa, C. (2015). Proton intensity spectra during the solar energetic particle events of May 17, 2012 and January 6, 2014. *Astronomy and Astrophysics*, *576*, A120. https://doi.org/10.1051/0004-6361/201424874

Lario, D., Aran, A., Gómez-Herrero, R., Dresing, N., Heber, B., Ho, G. C., et al. (2013). Longitudinal and radial dependence of solar energetic particle peak intensities: STEREO, ACE, GOES, and MESSENGER observations. *The Astrophysical Journal*, *767*(1), 41. https://doi.org/10.1088/0004-637X/767/1/41

Leske, R. A., Mewaldt, R. A., Stone, E. C., & von Rosenvinge, T. T. (2001). Observations of geomagnetic cutoff variations during solar energetic particle events and implications for the radiation environment at the Space Station. *Journal of Geophysical Research*, *106*, 30,011–30,022. https://doi.org/10.1029/2000JA000212

Matthiä, D., Schaefer, M., Meier, M. M., & M. M. (2015). Economic impact and effectiveness of radiation protection measures in aviation during a ground level enhancement. *Journal of Space Weather and Space Climate*, *5*, A17. https://doi.org/10.1051/swsc/2015014

Mauk, B., Fox, N., Kanekal, S., Kessel, R., Sibeck, D., & Ukhorskiy, A. (2013). Science objectives and rationale for the Radiation Belt Storm Probes mission. *Space Science Reviews*, *179*(1-4), 3–27. https://doi.org/10.1007/s11214-012-9908-y

Mazur, J., Friesen, L., Lin, A., Mabry, D., Katz, N., Dotan, Y., et al. (2012). The Relativistic Proton Spectrometer (RPS) for the Radiation Belt Storm Probes Mission. *Space Science Reviews*, *179*(1-4), 221–261. https://doi.org/10.1007/s11214-012-9926-9

Menderhall, M. H., & Weller, R. A. (2012). A probability-conserving cross-section biasing mechanism for variance reduction in Monte Carlo particle transport calculations. *Nuclear Instruments and Methods in Physics Research A*, *667*, 38–43. https://doi.org/10.1016/j.nima.2011.11.084

Mertens, C. J., Kress, B. T., Wiltberger, M., Blattnig, S. R., Slaba, T. S., Soloman, S. C., & Engel, M. (2010). Geomagnetic influence on aircraft radiation exposure during a solar energetic particle event on October 2003. *Space Weather*, *8*, S03006. https://doi.org/10.1029/2009SW00487

Morley, S. K., Brito, T. V., & Welling, D. T. (2018). Measures of model prediction quality based on the log accuracy ratio. *Space Weather*, *16*. https://doi.org/10.1002/2017SW001669

Morley, S. K., Sullivan, J. P., Carver, M. R., Kippen, R. M., Freidel, R. H. W., Reeves, G. D., & Henderson, M. G. (2017). Energetic particle data from the global positioning system constellation. *Space Weather*, *15*, 283–289. https://doi.org/10.1002/2017SW001604

Morley, S. K., Sullivan, J. P., Henderson, M. G., Blake, J. B., & Baker, D. N. (2016). The Global Positioning System constellation as a space weather monitor: Comparison of electron measurements with Van Allen Probes data. *Space Weather*, *14*, 76–92. https://doi.org/10.1002/2015SW001339

Mueller, J. T., Maldonado, H., & Driesman, A. S. (2003). Stereo: The challenges. *Acta Astronautica*, *53*(4-10), 729–738. https://doi.org/10.1016/S0094-5765(03)00122-X

Nesse Tyssøy, H. N., Stadsnes, J., Søraas, F., & Sørbø, M. (2013). Variations in cutoff latitude during the January 2012 solar proton event and implication for the distribution of particle energy deposition. *Geophysical Research Letters*, *40*, 4149–4153. https://doi.org/10.1002/grl.50815

Paassilta, M., Osku, R., Vainio, R., Papaioannou, A., Siipola, R., Riihonen, E., et al. (2017). Catalogue of 55-80 MeV solar proton events extending through solar cycles 23 and 24. *Journal of Space Weather and Space Climate*, *7*, A14. https://doi.org/10.1051/swsc/2017013

Panametrics (1979). Energetic particle sensor telescope calibration work, PANA-GOESP-CR2. Retrieved from https://www.ngdc.noaa.gov/stp/satellite/goes/documentation.html

Panametrics (1980). Energetic particle sensor dome calibration work, PANA-GOESP-CR3. Retrieved from https://www.ngdc.noaa.gov/stp/satellite/goes/documentation.html

Paularena, K. I., & King, J. H. (1999). NASA's IMP-8 spacecraft. In D. G. Sibeck & K. Kudela (Eds.), *Interball in the ISTP Program: Studies of the solar wind-magnetosphere-ionosphere interaction* (1–10 pp.). Dordrecht, Boston: Kluwer. Retrieved from ftp://space.mit.edu/pub/plasma/publications/kip_kosice_imp/kip_kosice_imp.withthumbs.pdf

Press, W. H., Teukolsky, S. A., Vettering, W. T., & Flannery, B. P. (1992). Numerical recipes. In *C: The Art of Scientific Computing* (pp. 490, 521–522). Cambridge, UK: Cambridge University Press.

Reames, D. V. (1995). Solar energetic particles: A paradigm shift. *Reviews of Geophysics*, *33*, 585–589. https://doi.org/10.1029/95RG00188

Reames, D. V. (2009). Solar energetic-particle release times in historic ground-level events. *The Astrophysical Journal*, *706*(1), 844–850. https://doi.org/10.1088/0004-637X/706/1/844

Rodriguez, J. V., Krosschell, J. C., & Green, J. C. (2014). Intercalibration of GOES 8-15 solar proton detectors. *Space Weather*, *12*, 92–109. https://doi.org/10.1002/2013SW000996

Rodriguez, J. V., Sandberg, I., Mewaldt, R. A., Daglis, I. A., & Jiggens, P. (2017). Validation of the effect of cross-calibrated GOES solar proton effective energies on derived integral fluxes by comparison with STEREO observations. *Space Weather*, *15*, 290–309. https://doi.org/10.1002/2016SW001533

Sandberg, I., Jiggens, P., Heynderickx, D., & Daglis, I. A. (2014). Cross calibration of NOAA GOES solar proton detectors using corrected NASA IMP-8/GME data. *Geophysical Research Letters*, *41*, 4435–4441. https://doi.org/10.1002/2014GL060469

Sauer, H. H., & Wilkinson, D. C. (2008). Global mapping of ionospheric HF/VHF radio wave absorption due to solar energetic protons. *Space Weather*, *6*, S12002. https://doi.org/10.1029/2008SW000399

Sen, P. K. (1968). Estimates of the regression coefficient based on Kendall's Tau. *Journal of the American Statistical Association*, *63*(324), 1379–1389. https://doi.org/10.1080/01621459.1968.10480934

Stone, E. C., Frandsen, A. M., Mewaldt, R. A., Christian, E. R., Margolies, D., Ormes, J. F., & Snow, F. (1998). The advanced composition explorer. *Space Science Reviews*, *86*(1/4), 1–22. https://doi.org/10.1023/A:1005082526237

Thakur, N., Gospalswamy, N., Xie, H., Mäkelä, P., Yashiro, S., Akiyama, S., & Davila, J. M. (2014). Ground level enhancement in the 2014 January 6 solar energetic particle event. *The Astrophysical Journal*, *790*(1), L13. https://doi.org/10.1088/2041-8205/790/1/L13

Tsurutani, B. T., Echer, E., Shibata, K., Verkhoglyadova, O. P., Mannucci, A. J., Gonzalez, W. D., et al. (2014). The interplanetary causes of geomagnetic activity during the 7-17 March 2012 interval: A CAWSES II overview. *Journal of Space Weather and Space Climate*, *4*, A02. https://doi.org/10.1051/swsc/2013056

Tylka, A. J., Adams, J. H. Jr., Boberg, P. R., Brownstein, B., Dietrich, W. F., Flueckiger, E. O., et al. (1997). CREME96: A revision of the cosmic ray effects on micro-electronics code. *IEEE Transactions on Nuclear Science*, *44*(6), 2150–2160. https://doi.org/10.1109/23.659030

United States Treaties and Other International Agreements (1963). Treaty banning nuclear weapon tests in the atmosphere, in outer space, and under water, (U.S.T, 1950–1982). [Retrieved from https://www.state.gov/t/isn/4797.htm.]

von Clarmann, T., Funke, B., López-Puertas, M., Kellmann, S., Linden, A., Stiller, G. P., et al. (2013). The solar proton events in 2012 as observed by MIPAS. *Geophysical Research Letters*, *40*, 2339–2343. https://doi.org/10.1002/grl.50119

Weller, R. A., Mendenhall, M. H., Reed, R. A., Schrimpf, R. D., Warren, K. M., Sierawki, B. D., & Massengill, L. M. (2010). Monte Carlo simulation of single event effects. *IEEE Transactions on Nuclear Science*, *51*(4), 1726–1746.

Wilcox, R. R. (1998). How many discoveries have been lost by ignoring modern statistical methods? *The American Psychologist*, *53*(3), 300–314. https://doi.org/10.1037/0003-066X.53.3.300

von Rosenvinge, T., Richardson, I., Reams, D., Cohen, C., Cummings, A., Leske, R., et al. (2009). The solar energetic particle event of 14 December 2006. *Solar Physics*, *256*(1-2), 443–462. https://doi.org/10.1007/s11207-009-9353-6